Electronic Supporting Information

Multifunctional organophosphorus ligand-templated poly(polyoxotungstate) with potential in building genosensor for thalassemia genetic detection

Wenshu Zhang,[b] Zixu Wang,[b] Mengya Cao,[b] Dan Wang,*[,a,b] Lijuan Chen,*[,b] and Junwei Zhao*[,b]

[a]*School of Pharmacy and Henan Province Engineering Research Center of High Value Utilization to Natural Medical Resource in Yellow River Basin, Henan University, Kaifeng 475004, China*
[b]*Henan Key Laboratory of Polyoxometalate Chemistry, College of Chemistry and Molecular Sciences, Henan University, Kaifeng, Henan 475004, China*
E-mail: wangdan@henu.edu.cn, ljchen@henu.edu.cn, zhaojunwei@henu.edu.cn

1−PEDOT/GCE. Here, current density (j) = CV current / area of the working electrode, $\Delta j = (j_{0.37\ V,\ high} - j_{0.37\ V,\ low}) / 2$, electrochemical double layer capacitance (C_{dl}) = the slope of the linear fitting line in (c).

Fig. S20 (a) The DPV curves of bare GCE stored for different times at room temperature. (b) Variation of relative DPV values of bare GCE stored for different times at room temperature. (c) The DPV curves of **1**−PEDOT film modified GCE stored for different times at room temperature. (d) Variation of relative DPV values of **1**−PEDOT film modified GCE stored for different times at room temperature.

Fig. S21 DPV curves of Au/**1**−PEDOT/GCEs with different electrochemical-deposition times of Au NPs.

Fig. S22 (a) The XPS spectrum of the Au/**1**−PEDOT film. (b) The XPS spectrum of the Au/**1**−PEDOT film for Au 4f.

Fig. S23 The AFM image of the Au/**1**−PEDOT film on the ITO substrate (the electrochemical deposition time: 80 s).

Fig. S24 SEM-EDS elemental mapping of the Au/**1**−PEDOT film on the ITO substrate at the 1 μm scale.

Fig. S25 DPV curves of pDNA/Au/**1**−PEDOT/GCEs with different incubation times.

Fig. S26 DPV curves of pDNA/Au/**1**−PEDOT/GCEs with different pDNA concentrations.

Fig. S27 DPV curves of dhDNA/Au/**1**−PEDOT/GCEs with different hybridization times between pDNA and tDNA.

Fig. S28 CV curves of bare GCE, **1**−PEDOT/GCE, Au/**1**−PEDOT/GCE, pDNA/Au/**1**−PEDOT/GCE and dhDNA/Au/**1**−PEDOT/GCE in Fe−PBS solution (pH = 7.4).

Fig. S29 DPV curves of five **1**-based GSs for 5×10^{-11} mol L^{-1} tDNA.

Fig. S30 DPV curves of different sequences of complementary DNA (cDNA) fragments on **1**-based GSs (left) and difference of current peaks ($\Delta I = I - I_0$, where I and I_0 refer to the current peaks with or without cDNA fragment detected), respectively (right). All samples have a concentration of 5×10^{-11} mol L^{-1}.

Fig. S31 DPV Current curves of **1**-based GSs for the tDNA detection in the presence of different interferents. (A = tDNA, B = ncsDNA + tDNA, C = tbmDNA + tDNA, D = dbmDNA + tDNA, E = ncsDNA + tbmDNA + tDNA, F = ncsDNA + dbmDNA + tDNA, G = dbmDNA + tbmDNA + tDNA, H = ncsDNA + tbmDNA + dbmDNA + tDNA, I: DPV curve of pDNA/Au/**1**−PEDOT/GCE, the concentrations of tDNA and interferents are 5×10^{-11} mol L^{-1}, pDNA = 1×10^{-7} mol L^{-1}).

Table S1. Crystallographic data and structure refinements for **1.**

Table S2. Comparison of the sensitivity of different sensors for detecting β-thalassemia gene.

1. Materials and measurements

$Na_2WO_4·2H_2O$, $Pr(NO_3)_3·6H_2O$, thylenediamine tetramethylphosphoric acid (H_8EDATMPA), antimony chloride, $K_3[Fe(CN)_6]$, $K_4[Fe(CN)_6]·3H_2O$, KCl, tris(hydroxymethyl)methylaminomethane (Tris), sodium hydroxide (NaOH), sodium dihydrogen phosphate (NaH_2PO_4), dibasic sodium phosphate (Na_2HPO_4) and KNO_3 were purchased from Sparke Chemical Co. Ltd. (Zhengzhou, Henan). Dimethylamine hydrochloride, 3, 4–ethylenedioxythiophene (EDOT), chloroauric acid ($HAuCl_4$) were purchased from Aladdin (Shanghai, China). Hydrochloric acid (HCl) was purchased from Haohua Chemical Co. Ltd. (Luoyang, Henan). The antisense strand of human β-thalassemia gene (tDNA) and its complementary DNA strand (pDNA), non-complementary sequences (ncs), double-base mismatched DNA (dbmDNA) and three-base mismatched DNA (tbmDNA) were bought from Shanghai Sangon Biological Engineering Technological Co. Ltd. (China) with the following sequences: pDNA: 5'–SH–ACTTCAGGATGAGTCTATGG–3'. tDNA: 5'–CCATAGACTCATCCTGAAGT–3'. ncs: 5'–AATCTCATGGCCGATTCGTT –3'. dbmDNA: 5'–CGATTGACTCATCCTGAAGT–3'. tbmDNA: 5'–CGATTGACACATCCTGAAGT–3'. All the DNA were dissolved in deionized water.

C, H and N elemental contents were performed on a Vario EL Cube CHNS analyzer. Inductively coupled plasma atomic emission spectrometry (ICP–AES) was performed on a Perkin–Elmer Optima 2100DV ICP mass spectrometer. IR spectra were recorded on a Bruker VERTEX 70 IR spectrometer using KBr pellets in the range of 400–4000 cm^{-1}. Powder X-ray diffraction (PXRD) pattern was obtained on a Bruker D8 ADVANCE apparatus using Cu Kα radiation (λ = 1.54056 Å) with a scan range (2θ) of 3.5 – 50° at 293 K. The thermogravimetric (TG) analysis was performed under N_2 atmosphere on a Mettler Toledo TGA/DSC 3+ thermal analyzer (temperature range: 25–1000 °C, heating rate: 10 °C min^{-1}). Electrospray ionization mass spectrometry (ESI-MS) was performed on an AB SCIEX Triple TOF 4600 instrument. Ultraviolet–visible (UV–vis) absorption spectra were recorded on a Mapada UV-6100 double beam spectrophotometer. X-ray photoelectron spectroscopy (XPS) measurements were conducted using a ThermoFischer ESCALAB 250X instrument. Atomic force microscopy (AFM) images were collected on a scanning probe microscope Dimension Icon (Bruke). Scanning electron microscopy (SEM) images and energy-dispersive spectrometer (EDS) patterns were obtained by JEOL JSM-7610F PLUS. Atomic force microscopy images were collected on a scanning probe microscope Bruke Dimension Icon. Raman spectroscopy was performed on Edinburgh RM5 Raman spectrometer with an excitation laser at 532 nm.

2. Experimental procedures

2.1 Synthesis of $[H_2N(CH_3)_2]_5Na_{11}H_9[(HEDATMPA)SbW_{15}O_{50}]\{[PrW_4O_{10}][B\text{-}\alpha\text{-}SbW_9O_{33}]_2·38H_2O$ (1)

The $Na_9[B\text{-}\alpha\text{-}SbW_9O_{33}]·19.5H_2O$ precursor was prepared according to the previous reference.[1] $Na_9[B\text{-}\alpha\text{-}SbW_9O_{33}]·19.5H_2O$ (2.502 g, 0.871 mmol), $Na_2WO_4·2H_2O$ (6.000 g, 18.190 mmol), H_8EDATMPA (0.203 g, 0.467 mmol) and dimethylamine hydrochloride (1.750 g, 21.460 mmol) were simultaneously dissolved in 25 mL deionized water. Then, a Sb^{3+} solution (700 μL, 1.0 mol L^{-1}) (prepared by dissolving 13.700 g $SbCl_3$ in 60 mL 6.0 mol L^{-1} HCl) was added into the reaction system. After this mixed solution was stirred for 5 min, the pH of solution was adjusted to 5.0 using 6.0 mol L^{-1} HCl. Whereafter, $Pr(NO_3)_3·6H_2O$ (0.200 g, 0.460 mmol) was introduced into the reaction solution, and the acidity of the reaction system was adjusted to 5.0 by 2.0 mol L^{-1} NaOH. After being stirred for another 30 min, the mixture was kept in a water bath (90 °C) for 2 h and then filtered after being cooled to room temperature. It should be pointed that, during the process of solvent evaporation, colorless crystals appeared after about ten days as by-products, which should be removed

by filtration. Finally, light green rectangular crystals could be collected after nearly fifteen days with a yield of 21.7% (calculated based on the dosage of Pr^{3+}).

2.2 Preparation of 1–PEDOT film on GCE or ITO and related tests

The **1**–PEDOT film was conducted by electropolymerization through cyclic voltammetry techinique in a solution containing 0.2 mmol L^{-1} **1**, 0.01 mol L^{-1} EDOT and 0.02 mol L^{-1} $NaClO_4$ at a scan rate of 0.10 V s^{-1} for a certain number of cycles (0 / 10 / 20 / 30 / 40 / 50 / 60 cycles). AFM, SEM and XPS tests were carried out with indium-tin oxide (ITO) as the substrate for the **1**–PEDOT film. The cyclic voltammetry (CV) tests (scan rate: 0.10 V s^{-1}) were carried out in 0.5 mol L^{-1} CH_3COOH–CH_3COONa buffer (pH = 4.5) or 0.10 mol L^{-1} phosphate buffered saline containing 0.01 mol L^{-1} $K_3[Fe(CN)_6]/K_4[Fe(CN)_6]$ (1:1) and 1.0 mol L^{-1} KCl (Fe–PBS, pH = 7.4). The differential pulse voltammetry (DPV) measurement (amplitude: 0.05 V) of **1**–PEDOT GCE was performed in Fe–PBS solution (pH = 7.4) at room temperature. The GCE modified by different materials were tested by CV technology with different sweep speed (0.02 V s^{-1} to 0.20 V s^{-1}) in the voltage range of 0.32–0.42 V in Fe–PBS solution (pH = 7.4) to calculate the electrochemically active surface area (ECSA).

2.3 Preparation of Au/1–PEDOT/GCE

The Au modified **1**–PEDOT/GCE (Au/**1**–PEDOT/GCE) was obtained by electrodeposition of gold nanoparticles on **1**–PEDOT/GCE in $AuCl_4^-$ solution (1 mL $HAuCl_4$ (1.00 g L^{-1}) solution and 1.010 g KNO_3 were used to prepare 100.0 mL $AuCl_4^-$ solution by using ultra-pure water) of −0.2 V (vs. Ag/AgCl). The electrodeposition time was 20 / 40 / 60 / 80 / 100/ 120 s. It provides the necessary condition for further pDNA binding through Au–S bond interaction.

2.4 Preparation of pDNA/Au/1–PEDOT/GCE (1-based GS)

5 μL pDNA was dropped onto the Au/**1**–PEDOT/GCE surface, which was maintained for some time at room temperature under humid condition, leading to the pDNA/Au/**1**–PEDOT/GCE. After the pDNA/Au/**1**–PEDOT/GCE was washed by using ultra-pure water, the modified GCE was then immersed in 20 μL of 2.0 wt% bovine albumin (BSA) (0.020g of BSA was dissolved in 10 mL deionized water) for 20 min to eliminate the nonspecific binding pDNA.

2.5 Optimization of experimental conditions

(1) The incubation time of pDNA: 5 μL of 1×10^{-8} mol L^{-1} pDNA was dropped onto the Au/**1**–PEDOT/GCE surface, and DPV curves of different incubation time (0.5 / 1.0 / 1.5 / 2.0 / 2.5 / 3.0 h) of the pDNA/Au/**1**–PEDOT/GCEs were got in Fe–PBS solution (pH = 7.4).

(2) The concentration of pDNA: 5 μL pDNA of different concentrations ($1 \times 10^{-9}/1 \times 10^{-8}/1 \times 10^{-7}/1 \times 10^{-6}/1 \times 10^{-5}$ mol L^{-1}) were separately dropped onto the Au/**1**–PEDOT/GCEs surface and their DPV signals were tested in Fe–PBS solution (pH = 7.4) 2 h later.

(3) The hybridization time between pDNA and tDNA: 10 μL of 1×10^{-11} mol L^{-1} tDNA was dropped onto the pDNA/Au/**1**–PEDOT/GCE surface, stewing for a period of time in the range of 10 to 60 min (10 / 20 / 30 / 40 / 50 / 60 min), and the corresponding current signals were tested in Fe–PBS solution (pH = 7.4).

2.6 Electrochemical detection of tDNA by 1-based GS

For the tDNA detection, 10 μL of tDNA solution with different concentrations (1×10^{-12} / 5×10^{-12} / 1×10^{-11} / 5×10^{-12} / 1×10^{-10} / 5×10^{-10} / 1×10^{-9}/ 5×10^{-9} mol L^{-1}) were dropped onto the surface of pDNA/Au/**1**–PEDOT/GCEs for 30 min under the most suitable conditions.

2.7 Electrochemical measurements

All electrochemical correlation tests are performed using with a three-GCE system (modified GCE or ITO glass as working electrode, Ag/AgCl as reference electrode, and platinum column electrode as counter electrode). All potentials in this work are referenced to the Ag/AgCl electrode. Without special instructions, CV and DPV were recorded in Fe–PBS solution (pH = 7.4).

Fe–PBS: 0.823 g $K_3[Fe(CN)_6]$, 1.056 g $K_4[Fe(CN)_6]$ and 37.275 g KCl were dissolved in 250 mL ultrapure water, and then transferred into a 500 mL volumetric flask. Then the resulting solution was diluted by using PBS (pH = 7.40) to 500 mL.

2.8 X-ray crystallography

Diffraction intensity data of **1** were collected on a Bruker D8 Venture Photon II diffractometer using monochromated Mo Kα radiation (λ = 0.71073 Å) at 150 K. Routine Lorentz and polarization corrections were applied and a multi-scan absorption correction was utilized with the SADABS program. Direct methods were used to solve the structure, refined on F^2 by full-matrix least-squares method, using the SHELXTL–97 program.[2,3] Non-hydrogen atoms associated with water molecules were located from the difference Fourier map. All non-hydrogen atoms except for some sodium, carbon, oxygen atoms and water molecules. All H atoms connected to N and C atoms were generated geometrically and refined isotropically as a riding model using the default SHELXTL parameters. No hydrogen atoms associated with water molecules are located from the difference Fourier map. All non-hydrogen atoms are refined anisotropically except for some oxygen atoms and water molecules. However, there are still solvent accessible voids accessible solvent voids in the check cif report of crystal structure, suggesting that some lattice water molecules and counter cations should exist in the structure, which can't be found from the weak residual electron peaks. In the light of elemental analysis and TG analysis, two $[H_2(CH_3)_2]^+$ cations, nine protons and five lattice water molecules were directly added to the molecular formula of **1**. Element analysis (%): H, 1.37 (calcd. 1.23); C, 1.83 (calcd. 1.76); N, 1.13 (calcd. 1.15); Na, 2.43 (calcd. 2.32); W, 63.09 (calcd. 62.25); Pr, 1.45 (calcd. 1.29). The crystallographic data and structure refinements for **1** are demonstrated in Table S1. Crystallographic data for **1** reported in this paper has been deposited in the Cambridge Crystallographic Data Centre with CCDC 2253643 for **1**.

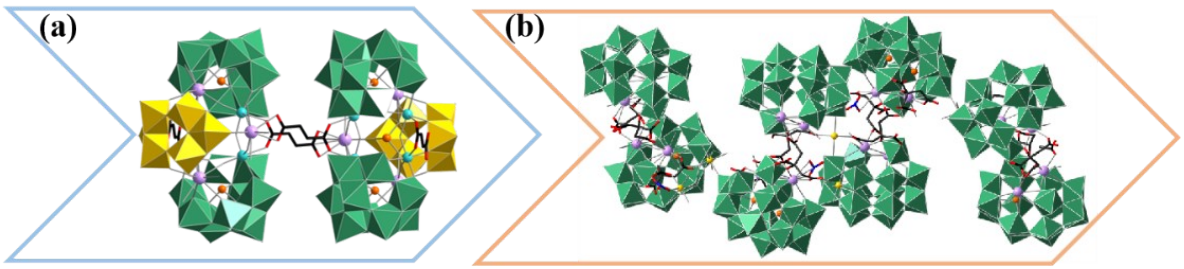

Fig. S1 (a,b) Two poly(POT) clusters with the help of organic ligand linkers.

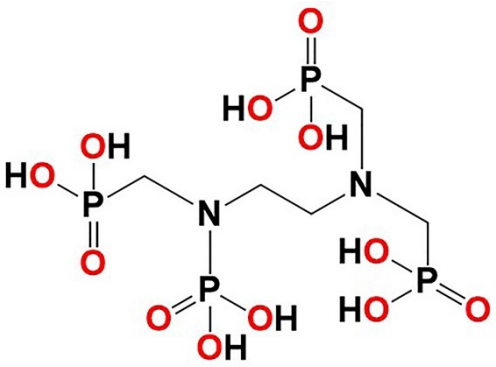

Fig. S2 View of the H_8EDATMPA ligand.

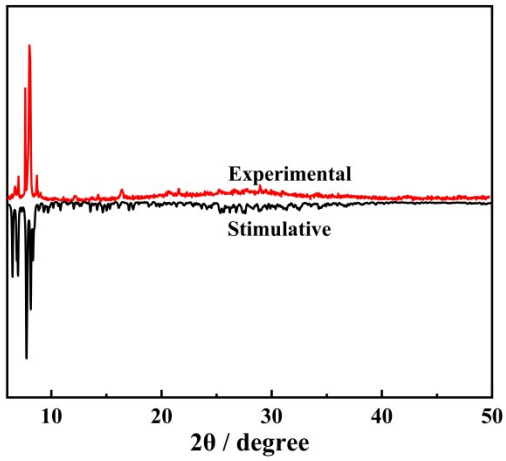

Fig. S3 Comparison of the PXRD pattern and the single-crystal XRD pattern of **1**.

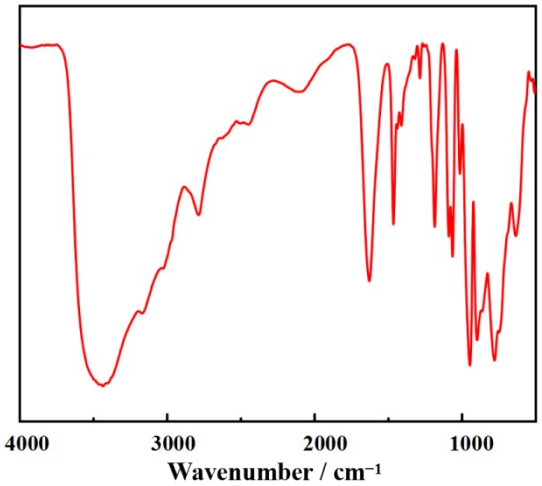

Fig. S4 The IR spectrum of **1**.

The IR spectrum of **1** is measured between 4000 and 400 cm^{-1} on a Bruker VERTEX 70 IR spectrometer by employing KBr pellets (Fig. S4). Obviously, the IR spectrum of **1** shows the characteristic vibration bands in the low wavenumber region (v < 1100 cm^{-1}), which demonstrates five main typical vibration peaks from lacunary (Sb^{III}, P^{V})-heteroatom-directing POT segments appearing at 1063, 952, 898, 785 and 711 cm^{-1}, which are separately attributed to the asymmetrical stretching vibrations of P^{V}–O, terminal W–O_t, corner-sharing W–O_b, edge-sharing W–O_c and Sb^{III}–O_a.[4,5] Moreover, one very strong and wide absorption band at 3468−3395 cm^{-1} could be found

which is on account of the O–H stretching vibration. The C–H bond stretching vibrations from $[H_2N(CH_3)_2]^+$ cations correspond to the weak absorption band located at 2802−2782 cm^{-1}. In the middle wavenumber region, one sharp absorption band at 1635–1628 cm^{-1} which is caused by the O–H bending vibration from lattice and coordination water molecules while the source of the weak band at 1466–1463 cm^{-1} is the C–H band bending vibration of $[H_2N(CH_3)_2]^+$ cations.

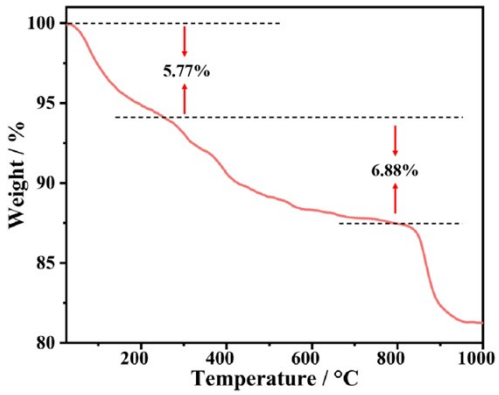

Fig. S5 The TG curve of **1**.

For the sake of exploring the thermal stability of **1**, the TG measurement was carried out from 25 to 1000 °C under a N_2 atmosphere at a heating rate of 10 °C min^{-1}. The TG curve suggests that **1** undergoes a three-step slow weight loss (Fig. S5). The first weight loss of 5.77% (calcd. 6.26 %) is attributed to the liberation of thirty-eight lattice water molecules. The second weight loss step of 6.88 % (calcd. 7.30 %) from 250 to 800 °C corresponds the removal of five dimethylamine groups, the dehydration of nine protons as well as the loss of six carbon dioxide and ten water molecules from the decomposition of the H_8EDATMPA ligand. After the temperature exceeds 800 °C, the weight loss stem from the sublimation of WO_3.

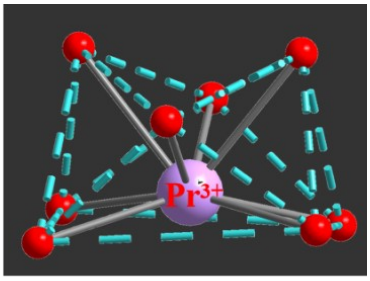

Fig. S6 Coordination environment of the $Pr1^{3+}$ ion.

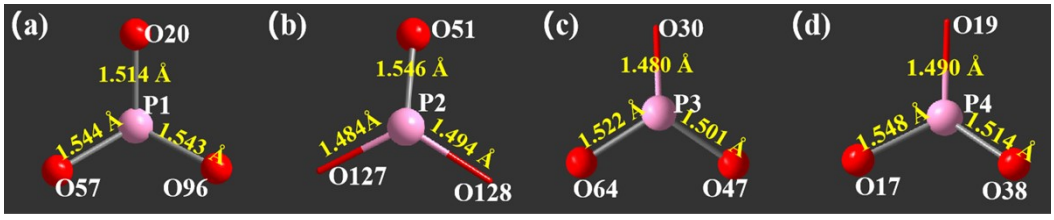

Fig. S7 (a–d) Coordination environments of $P1^V$, $P2^V$, $P3^V$ and $P4^V$ atoms of the organophosphonic acid. (The O atoms connected with W atoms are highlighted by spherical mode while the uncoordinated O atoms are highlighted by bond line mode)

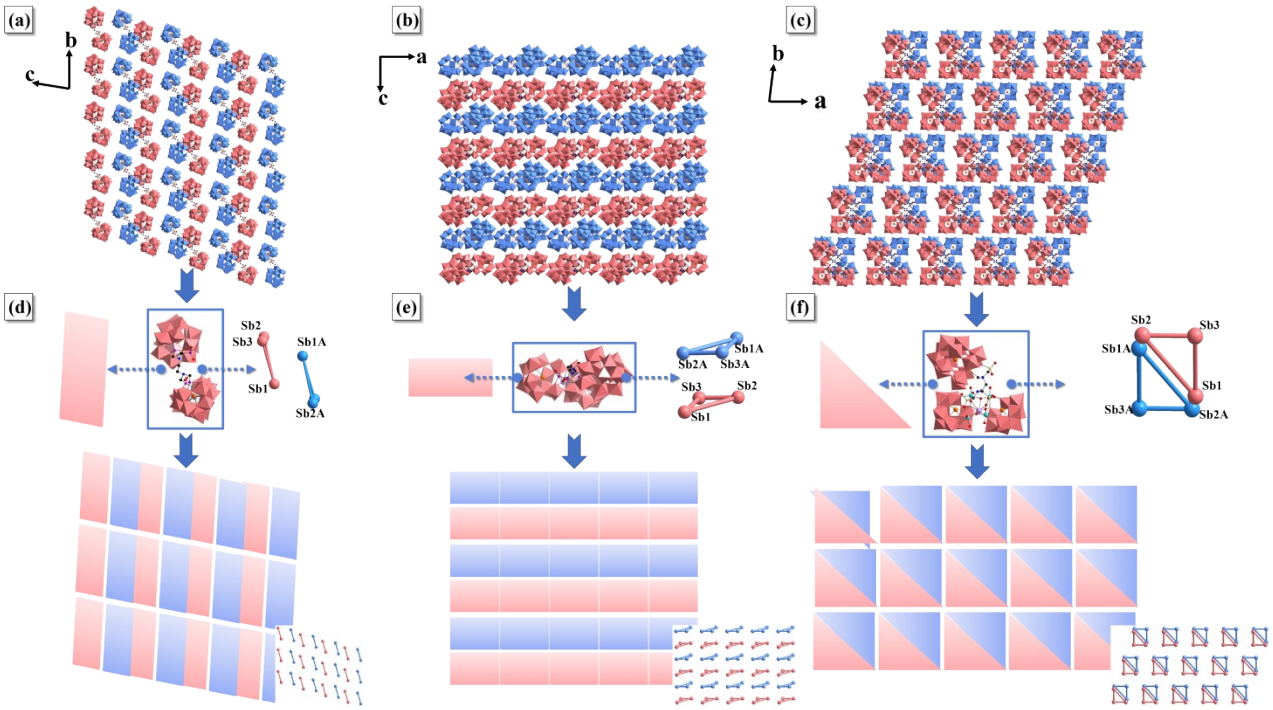

Fig. S8 (a–c) 3D spatial arrangements of **1a** polyanions viewed along the *a*, *b* and *c* axes. (d–f) 3D simplified arrangements of **1a** polyanions viewed along the *a*, *b* and *c* axes.

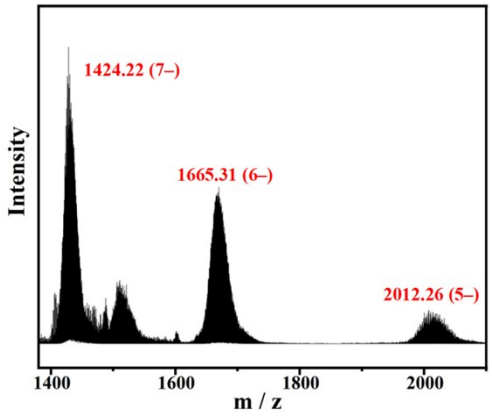

Fig. S9 The ESI–MS spectrum of **1** in aqueous solution.

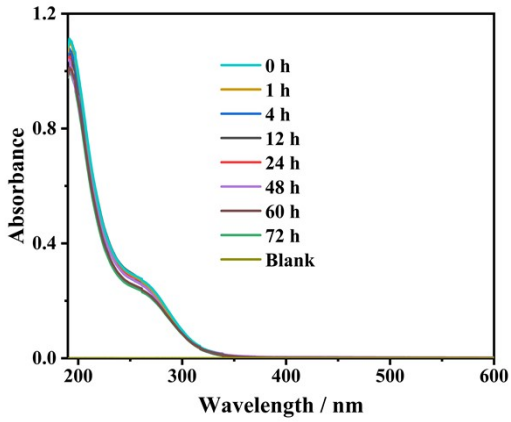

Fig. S10 The UV-vis spectra of **1** in aqueous solution collected at different time points.

Previous literatures have shown that UV-vis spectroscopy can be used as an effective method to study the stability of compounds in aqueous solution.[6,7] Therefore, the UV-vis spectra of **1** in aqueous solution were collected at 0 / 1 / 4 / 12 / 24 / 48 / 60 / 72 h. As illustrated in Fig. S10, the strong absorption band at ca. 192 nm can be assigned to the *p*π–*d*π charge transfer transitions of the O_t–W bonds, and the weak absorption band at about 270 nm can be attributed to the *p*π–*d*π charge transfer transitions of the $O_{b/c}$–W bonds. Apparently, the UV-vis spectra of **1** in aqueous solution are almost unchanged in 72 hours, indicating that the poly(POT) skeleton of **1** has good stability in aqueous solution.

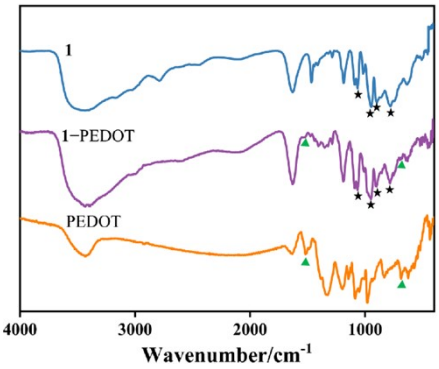

Fig. S11 Comparison of IR spectra of **1**, PEDOT and **1**–PEDOT.

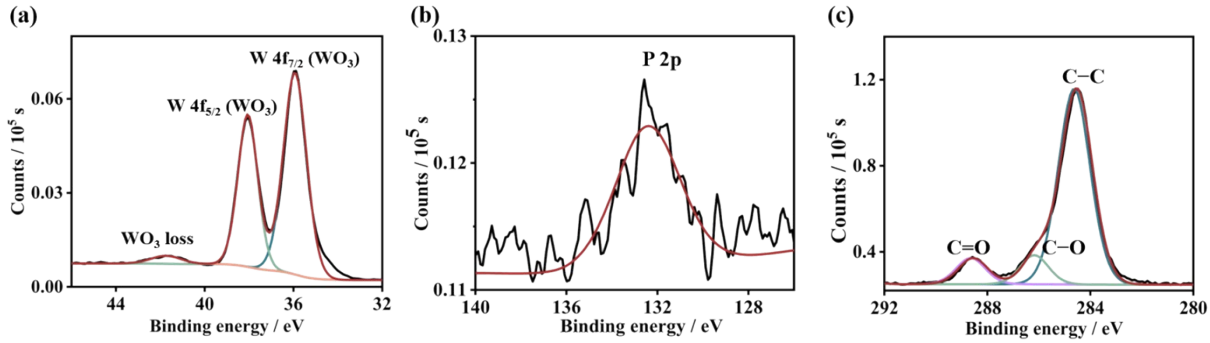

Fig. S12 XPS spectra of **1** for (a) W 4f, (b) P 2p, (c) C 1s.

From these XPS spectra of **1**, some characteristic peaks attributed to W (W $4f_{7/2}$: 35.9 eV, W $4f_{5/2}$: 38.0 eV), P (P 2p: 132.3 eV) and C (C–C: 284.9 eV, C–O: 286.5 eV and C=O: 288.4 eV) could be observed.[8–10]

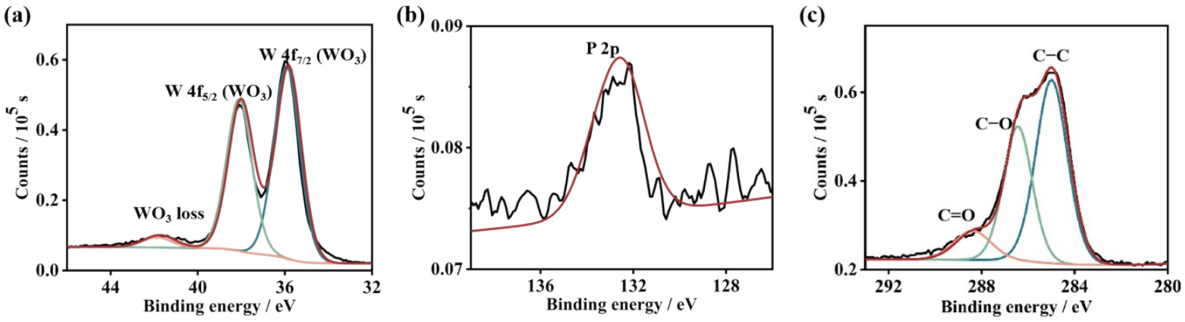

Fig. S13 XPS spectra of the **1**–PEDOT hybrid film for (a) W 4f, (b) P 2p and (c) C 1s.

From these XPS spectra of the **1**–PEDOT hybrid film, some characteristic peaks attributed to W (W $4f_{7/2}$: 35.9 eV, W $4f_{5/2}$: 38.1 eV), P (P 2p: 132.5 eV) and C (C–C: 285.0 eV, C–O: 286.5 eV and C=O: 288.4 eV) could be observed.[8–10]

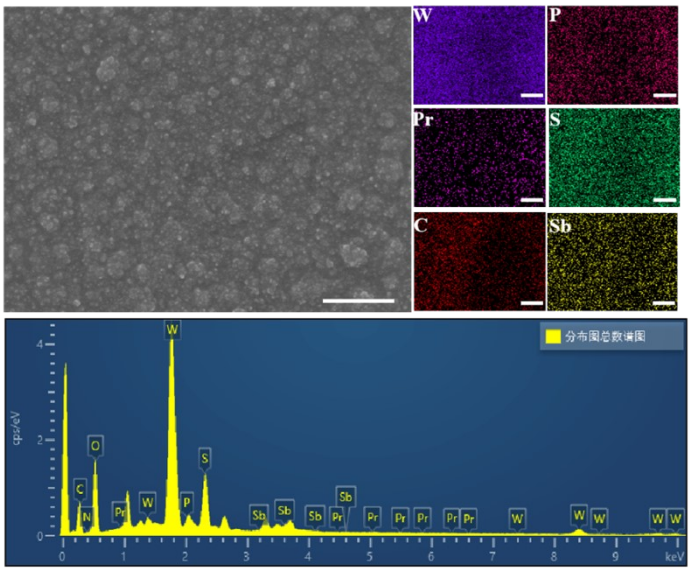

Fig. S14 SEM-EDS elemental mapping image of the **1**–PEDOT hybrid film on ITO glass at the 1 µm scale.

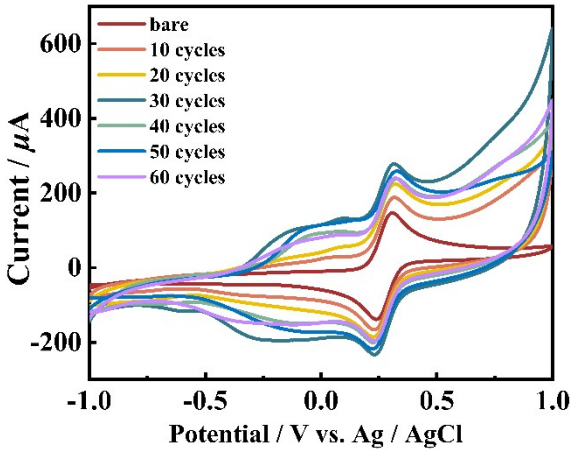

Fig. S15 CV curves of **1**–PEDOT/GCEs with different electropolymerization cycles in Fe–PBS solution (pH = 7.4).

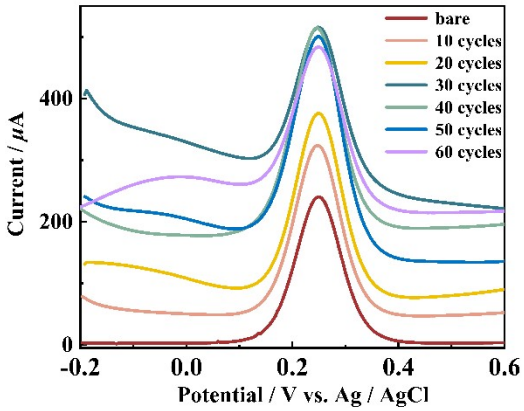

Fig. S16 DPV curves of **1**–PEDOT/GCEs with different electropolymerization cycles.

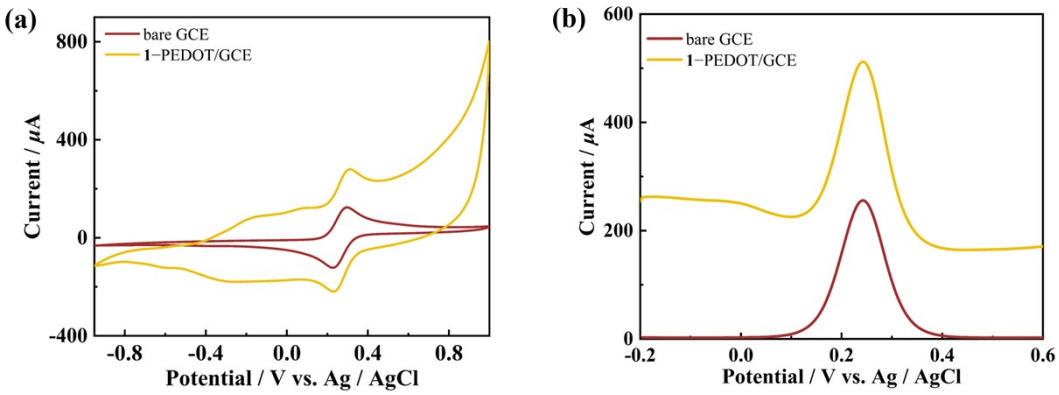

Fig. S17 (a) CV curves of bare GCE and **1**–PEDOT/GCE in Fe–PBS solution (pH = 7.4). (b) DPV curves of bare GCE and **1**–PEDOT/GCE in Fe–PBS solution (pH = 7.4).

As can be apparently seen from Fig. S17a, both the peak current and electroactive area of **1**–PEDOT/GCE significantly enhanced compared with those of bare GCE. At the same time, the DPV signal of **1**–PEDOT/GCE is much higher than that of bare GCE (Fig. S17b). Therefore, the **1**–PEDOT film modification significantly increases the conductivity of GCE.

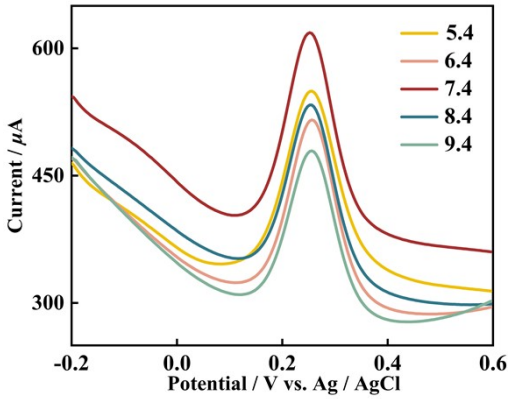

Fig. S18 DPV curves of **1**–PEDOT/GCE in 0.10 mol L^{-1} PBS solutions containing 0.01 mol L^{-1} 1:1 $[Fe(CN)_6]^{3-/4-}$ with different pH values (pH = 5.4 / 6.4 / 7.4 / 8.4 / 9.4).

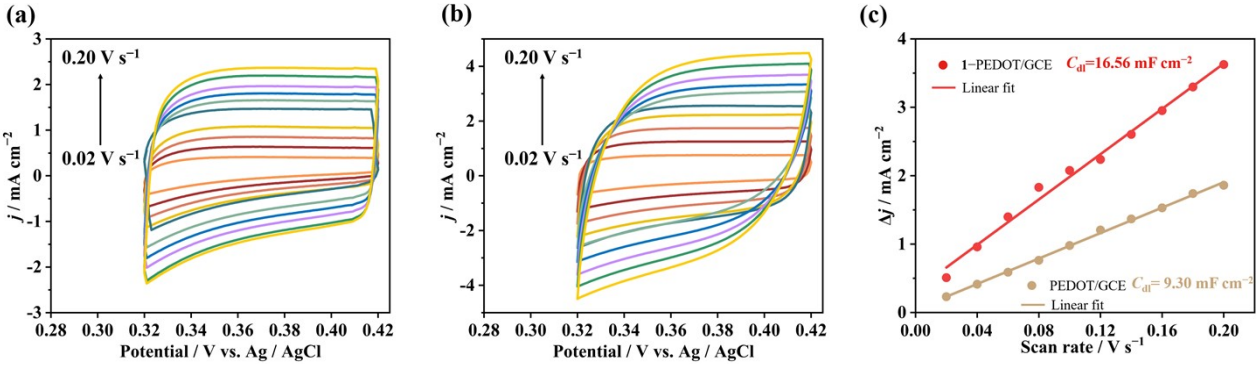

Fig. S19 (a) CV curves of PEDOT/GCEs in Fe–PBS solution (pH = 7.4) with scan rate in the range of 0.02–0.20 V s^{-1}. (b) CV curves of **1**–PEDOT/GCEs in Fe–PBS solution (pH = 7.4) with scan rate in the range of 0.02–0.20 V s^{-1}. (c) The linear relationship between Δj and scan rate at a given potential (0.37 V) and the C_{dl} of PEDOT/GCE and **1**–PEDOT/GCE. Here, current density (j) = CV current / area of the working electrode, $\Delta j = (j_{0.37\ V,\ high} - j_{0.37\ V,\ low}) / 2$, electrochemical double layer capacitance (C_{dl}) = the slope of the linear fitting line in (c).

It has been demonstrated that the electrochemically active surface area (ECSA) is positively proportional to C_{dl}.[11,12] As the C_{dl} of **1**–PEDOT/GCE (16.56 mF cm^{-2}) is larger than that of PEDOT/GCE (9.30 mF cm^{-2}), ECSA of of **1**–PEDOT/GCE is also larger. This indicates that the participation of **1** significantly improves the ECSA of the film-modified GCE.

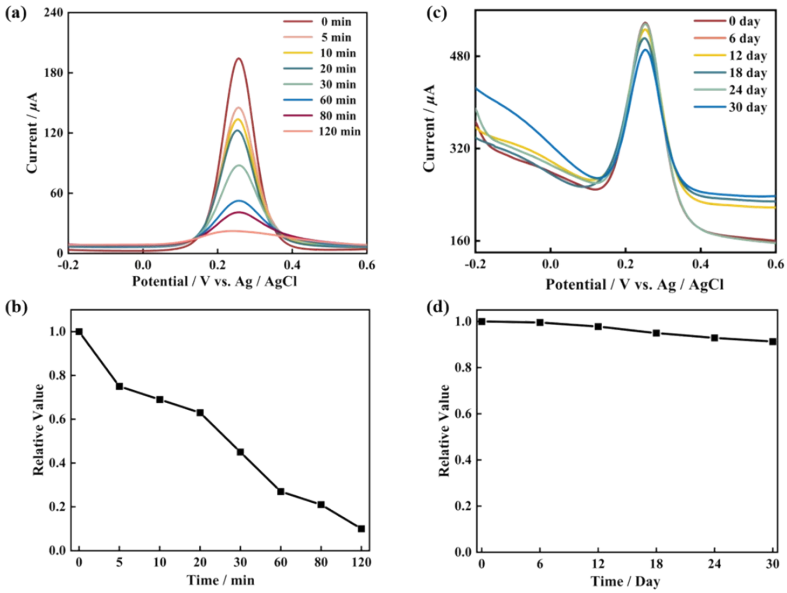

Fig. S20 (a) The DPV curves of bare GCE stored for different times at room temperature. (b) Variation of relative DPV values of bare GCE stored for different times at room temperature. (c) The DPV curves of **1**–PEDOT film modified GCE stored for different times at room temperature. (d) Variation of relative DPV values of **1**–PEDOT film modified GCE stored for different times at room temperature.

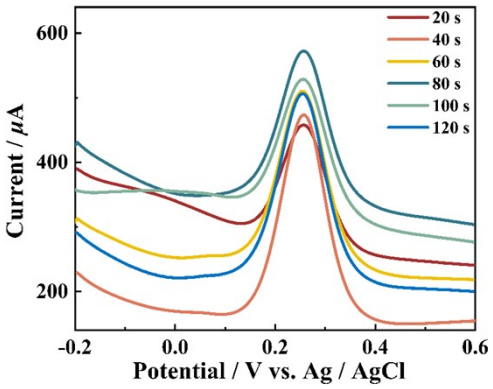

Fig. S21 DPV curves of Au/**1**–PEDOT/GCEs with different electrochemical-deposition times of Au NPs.

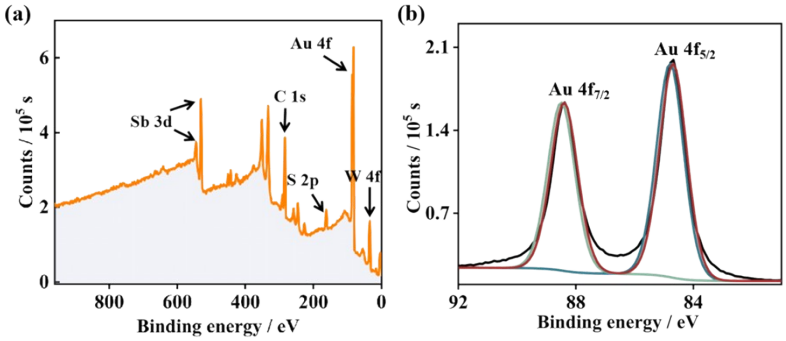

Fig. S22 (a) The XPS spectrum of the Au/**1**–PEDOT film. (b) The XPS spectrum of the Au/**1**–PEDOT film for Au 4f.

From this XPS spectrum, some characteristic peaks around 530 eV, 284 eV, 163 eV and 37 eV could be observed, which can be attributed to Sb 3d, C 1s, S 2p and W 4f of the **1**–PEDOT film. At the same time, two characteristic peaks of Au can be observed (Au $4f_{5/2}$: 84.8 eV, Au $4f_{7/2}$: 88.5 eV), demonstrating the deposition of Au NPs.[13]

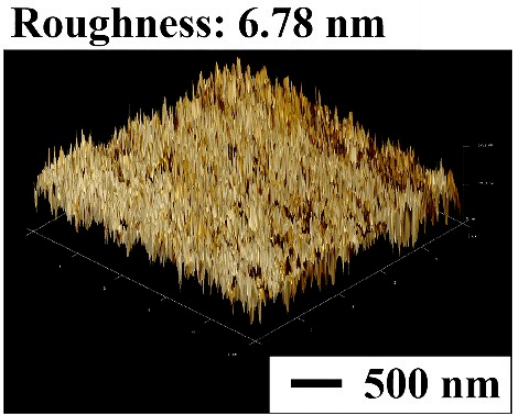

Fig. S23 The AFM image of the Au/**1**–PEDOT film on the ITO substrate (the electrochemical deposition time: 80 s).

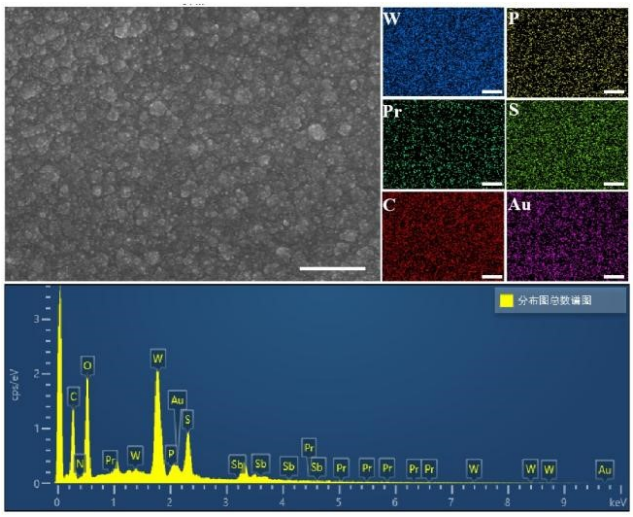

Fig. S24 SEM-EDS elemental mapping of the Au/**1**–PEDOT film on the ITO substrate at the 1 μm scale.

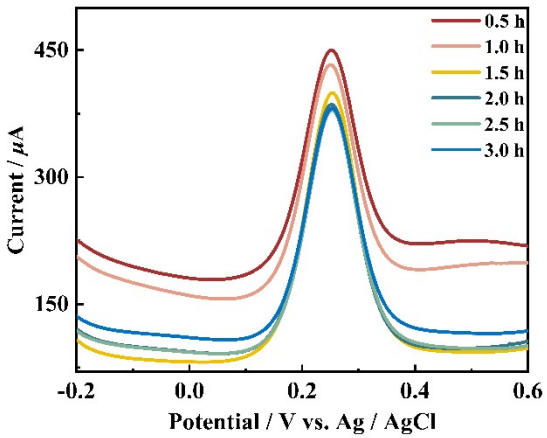

Fig. S25 DPV curves of pDNA/Au/**1**–PEDOT/GCEs with different incubation times.

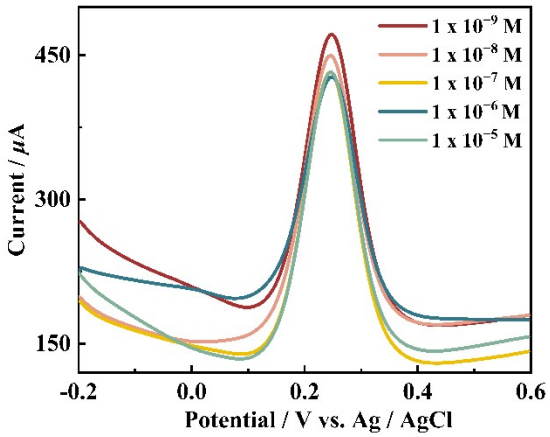

Fig. S26 DPV curves of pDNA/Au/**1**−PEDOT/GCEs with different pDNA concentrations.

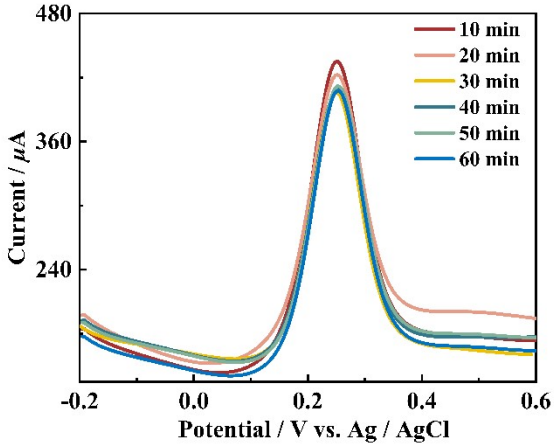

Fig. S27 DPV curves of dhDNA/Au/**1**−PEDOT/GCEs with different hybridization times between pDNA and tDNA.

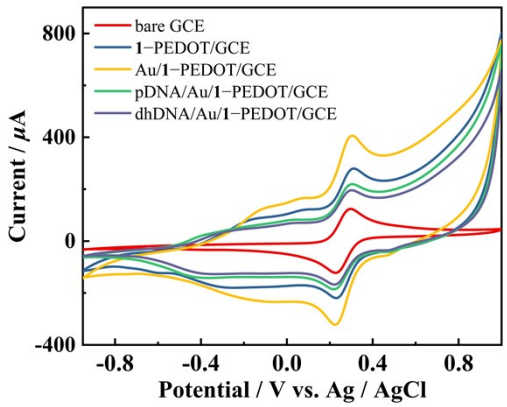

Fig. S28 CV curves of bare GCE, **1**−PEDOT/GCE, Au/**1**−PEDOT/GCE, pDNA/Au/**1**−PEDOT/GCE and dhDNA/Au/**1**−PEDOT/GCE in Fe−PBS solution (pH = 7.4).

It can be clearly seen from Fig. S28 that all the modified GCEs exhibit enhanced peak currents and electroactive areas compared with the bare GCE, demonstrating that the electrical conductivities of the modified electrodes increase. Moreover, the electrical conductivity of Au/**1**−PEDOT/GCE is much higher than that of **1**−PEDOT/GCE owing to the electrochemical deposition of Au on the electrode surface. After the electronegative pDNA is fixed on the surface of Au/**1**−PEDOT/GCE, the peak current and electroactive area of pDNA/Au/**1**−PEDOT/GCE decrease. Finally, the formation of double helix DNA by combining tDNA with pDNA leads to the further decreasing of the peak current and electroactive area.

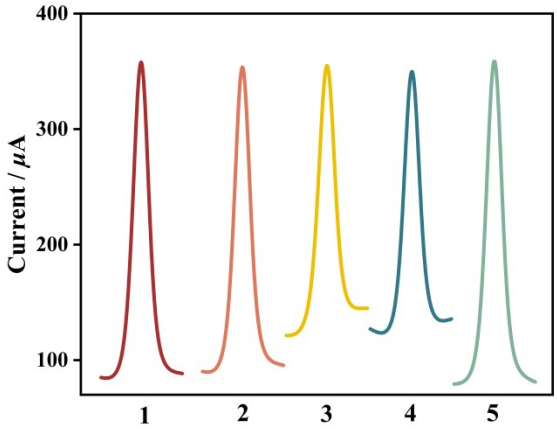

Fig. S29 DPV curves of five **1**-based GSs for 5×10^{-11} mol L^{-1} tDNA.

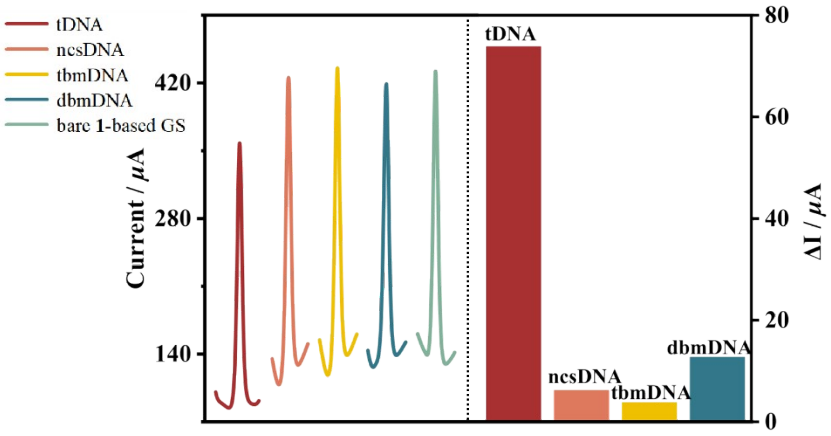

Fig. S30 DPV curves of different sequences of complementary DNA (cDNA) fragments on **1**-based GSs (left) and difference of current peaks ($\Delta I = I - I_0$, where I and I_0 refer to the current peaks with or without cDNA fragment detected), respectively (right). All samples have a concentration of 5×10^{-11} mol L^{-1}.

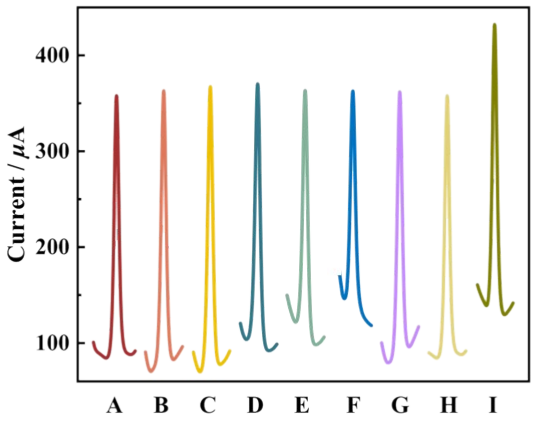

Fig. S31 DPV Current curves of **1**-based GSs for the tDNA detection in the presence of different interferents. (A = tDNA, B = ncsDNA + tDNA, C = tbmDNA + tDNA, D = dbmDNA + tDNA, E = ncsDNA + tbmDNA + tDNA, F = ncsDNA + dbmDNA + tDNA, G = dbmDNA + tbmDNA + tDNA, H = ncsDNA + tbmDNA + dbmDNA + tDNA, I: DPV curve of pDNA/Au/**1**–PEDOT/GCE, the concentrations of tDNA and interferents are 5×10^{-11} mol L^{-1}, pDNA = 1×10^{-7} mol L^{-1}).

Table S1. Crystallographic data and structure refinements for **1.**

	1
Empirical formula	$C_{16}H_{138}N_7Na_{11}O_{176}P_4Pr_4Sb_3W_{37}$
*F*w	10772.44
T (K)	150(2)
Crystal system	Triclinic
Space group	*P*–1
a (Å)	22.2168(8)
b (Å)	23.5667(9)
c (Å)	23.7350(9)
α (deg)	72.1850(10)
β (deg)	83.2620(10)
γ (deg)	69.6040(10)
V (Å^3)	11088.7(7)
Z	2
D_c (g·cm^{-3})	3.226
μ (mm^{-1})	19.819
F(000)	9460
Limiting indices	−26 ≤ *h* ≤ 26 −28 ≤ *k* ≤ 28 −28 ≤ *l* ≤ 28
Reflections collected / unique	136763 / 38891
R_{int}	0.0927
Data / restraints / parameters	38891 / 19 / 2078
GOF on F^2	1.029
R_1, wR_2 [$I > 2\sigma(I)$]	R_1 = 0.0589, wR_2 = 0.1432
R_1, wR_2 [all data]	R_1 = 0.1103, wR_2 = 0.1630

Table S2. Comparison of the sensitivity of different sensors for detecting β-thalassemia gene.

Electrochemical method	Target object	Limit of detection	Linear range	Ref.
DPV	Antisense strand of human β-thalassemia gene	6.0×10^{-14} mol L^{-1}	$1 \times 10^{-12} - 4 \times 10^{-10}$ mol L^{-1}	14
CV	Hemoglobin	2.9×10^{-7} mol L^{-1}	–	15
Linear sweep	Complementary	7.7×10^{-11} mol L^{-1}	–	16

voltammetry	polymerase chain reaction products			
DPV	Antisense strand of human β-thalassemia gene	2.6×10^{-13} mol L^{-1}	$1 \times 10^{-12} - 5 \times 10^{-9}$ mol L^{-1}	Our Work

References

1. M. Bösing, I. Loose, H. Pohlmann and B. Krebs, New strategies for the generation of large heteropolymetalate clusters: the *β*-B-SbW_9 fragment as a multifunctional unit, *Chem. Eur. J.,* 1997, **3**, 1232−1237.
2. G. M. Sheldrick, SHELXL-97, Program for Crystal Structure Refinement, University of Göttingen: Göttingen, Germany, 1997.
3. G. M. Sheldrick, SHELXS-97, Program for Crystal Structure Solution, University of Göttingen: Göttingen, Germany, 1997.
4. X. Xin, X. Y. Liu, D. Wang, X. J. Liu, L. J. Chen and J. W. Zhao, {HPO_3} and {WO_4} simultaneously induce the assembly of tri-Ln(III)-incorporated antimonotungstates and their photoluminescence behaviors, *Inorg. Chem*., 2021, **60**, 1037−1044.
5. S. S. Xie, J. Jiang, D. Wang, Z. G. Tang, R. F. Mi, L. J. Chen and J. W. Zhao, Tricarboxylic-ligand-decorated lanthanoid-inserted heteropolyoxometalates built by mixed-heteroatom-directing polyoxotungstate units: syntheses, structures, and electrochemical sensing for 17*β*-estradiol, *Inorg. Chem.*, 2021, **60**, 7536–7544.
6. H. Y. Zang, H. N. Miras, J. Yan, D. -L. Long and L. Cronin, Assembly and autochirogenesis of a chiral inorganic polythioanion Möbius strip via symmetry breaking, *J. Am. Chem. Soc.*, 2012, **134**, 11376–11379.
7. Y. Zhang, D. Wang, B. X. Zeng, L. J. Chen, J. W. Zhao and G. -Y. Yang, An unprecedented polyhydroxycarboxylic acid ligand bridged multi-Eu^{III} incorporated tellurotungstate and its luminescence properties, *Dalton Trans*., 2020, **49**, 8933–8948.
8. D. Wang, J. Jiang, M. Y. Cao, S. -S. Xie, Y. -M. Li, L. -J. Chen, J. -W. Zhao and G. -Y. Yang, An unprecedented dumbbell-shaped pentadeca-nuclear W−Er heterometal cluster stabilizing nanoscale hexameric arsenotungstate aggregate and electrochemical sensing properties of its conductive hybrid film-modified electrode, *Nano Res.*, 2022, **15**, 3628−3637.
9. X. F. Cui, Q. F. Li, Y. Li, F. H. Wang, G. Jin and M. H. Ding, Microstructure and corrosion resistance of phytic acid conversion coatings for magnesium alloy, *Appl. Surf. Sci.,* 2008, **255**, 2098−2103.
10. W. K. Wang, Y. H. Wu, Z. W. Jiang, M. Z. Wang, Q. C. Wu, X. Zhou and X. W. Ge, Formation mechanism of 3D macroporous graphene aerogel in alcohol-water media under gamma-ray radiation, *Appl. Surf. Sci.,* 2018, **427**, 1144−1151.
11. M. X. Li, Y. Zhu, N. Song, C. Wang and X. F. Lu, Fabrication of Pt nanoparticles on nitrogen-doped carbon/Ni nanofibers for improved hydrogen evolution activity, *J. Colloid Interface Sci.*, 2018, **514**, 199–207.
12. Q. He, Y. Y. Wan, H. L. Jiang, Z. W. Pan, C. Q. Wu, M. Wang, X. J. Wu, B. J. Ye, P. M. Ajayan and L. Song, Nickel vacancies boost reconstruction in nickel hydroxide electrocatalyst, *ACS Energy Lett.*, 2018, **3**, 1373−1380.
13. L. C. Wang, Y. M. Liu, M. Chen, Y. Cao, He. Y. He and K, N. Fan, MnO_2 nanorod supported gold nanoparticles with enhanced activity for solvent-free aerobic alcohol oxidation, *J. Phys. Chem. C*., 2008, **112**, 6981−6987.
14. M. -B. Gholivand and A. Akbari, A sensitive electrochemical genosensor for highly specific detection of thalassemia gene, *Biosensors and Bioelectronics*, 2019, **129**, 182−188.
15. H. S. Rafiq, B. Fatima, D. Hussain, A. Mohyuddin, S. Majeed, S. Manzoor, M. Imran, R. Nawaz, S. Shabbir, S. Mukhtar, M. N. Ashiq and M. Najam-ul-Haq, Selective electrochemical sensing of hemoglobin from blood of β-thalassemia major patients by tellurium nanowires-graphene oxide modified electrode, *Chem. Eng. J.*, 2021, **419**, 129706.
16. E. Hamidi-Asl, J. B. Raoof, N. Naghizadeh, H. Akhavan-Niaki, R. Ojani and A. Banihashemi, A bimetallic nanocomposite modified genosensor for recognition and determination of thalassemia gene, *Int. J. Biol. Macromol.,* 2016, **91**, 400−408.